

# Chirped-pulse oscillators: a unified standpoint

V. L. Kalashnikov

*Institut für Photonik, TU Wien, Gusshausstr. 27/387, A-1040 Vienna, Austria*

A. Apolonski

*Department für Physik der Ludwig-Maximilians-Universität München,*

*Am Coulombwall 1, 85748, Germany and*

*Institute of Automation and Electrometry, RAS, 630090 Novosibirsk, Russia*

## Abstract

A completely analytical and unified approach to the theory of chirped-pulse oscillators is presented. The approach developed is based on the approximate integration of the generalized nonlinear complex Ginzburg-Landau equation and demonstrates that a chirped-pulse oscillator is controlled by only two parameters. It makes it easy to trace spread of the real-world characteristics of both solid-state and fiber oscillators operating in the positive dispersion regime.

PACS numbers: 42.65.Re, 42.65.Tg, 42.65.Sf

## I. INTRODUCTION

High-energy laser oscillators nowadays allow high-intensity experiments such as direct gas ionization [1], where the level of intensity must be of the order of  $10^{14}$  W/cm<sup>2</sup>. One can expect soon pump-probe diffraction experiments with electrons and direct high-harmonic generation in gases and production of nm-scale structures at the surface of transparent materials. Each case calls for an intensity of the order of that demonstrated above or higher, which means generating tens up to hundreds of  $\mu$ J pulses at the fundamental MHz repetition rate of an oscillator [2]. From the examples above it can be seen that high repetition rates are preferable to kHz rates (now commercially available) because the signal rates in, for example, electron experiments are usually low and an improvement factor of  $10^3 - 10^4$  due to the higher repetition rate of the pulses significantly enhances the signal-to-noise ratio. In addition to this physical factor, existing kHz systems are more expensive, complex and less stable.

There are a few ways of increasing the oscillator pulse energy  $E$ , which is a product of the average power and the repetition period: by increasing the cavity length and/or increasing the power [3, 4, 5, 6, 7, 8]. The catch is that a long-cavity oscillator suffers from instabilities owing to nonlinear effects caused by the high pulse peak power  $P_0$ . The leverage is to stretch a pulse and thereby decrease its peak power below the instability threshold. Recent progress demonstrating the feasibility of this approach has been achieved for Ti:sapphire oscillators operating in both the negative- (NDR) [9, 10] and positive-dispersion regimes (PDR) [11, 12], for near-infrared Yb-doped solid-state oscillators operating in both the NDR [5, 8, 13] and the PDR [13, 14], and for fiber oscillators operating in the all-normal dispersion (ANDi; i.e. positive dispersion) regime [15, 16].

The fundamental difference between the NDR and PDR is that, in the former, the Schrödinger soliton develops [17]. The soliton width  $T$  and energy  $E$  can be expressed as [18]

$$T = \sqrt{|\beta|/\gamma P_0}, \quad E = 2 |\beta|/\gamma T, \quad (1)$$

where  $\gamma$  is the self-phase modulation (SPM) coefficient of a nonlinear medium (active crystal, fiber, air, etc.), and  $\beta$  is the net-group-delay-dispersion (GDD) coefficient of an oscillator. Since the peak power  $P_0$  has to be kept lower than the threshold value  $P_{th}$  in order to avoid

soliton destabilization, one can estimate the maximum attainable energy as  $E = 2P_{th}T$ . Energy scaling thus requires pulse stretching. However, the latter results from the substantial GDD growth (quadratically with energy, see Eq. (1)):

$$|\beta| = E^2\gamma/4P_{th}. \quad (2)$$

Hence, the pulse width increases linearly with energy (correspondingly, the spectrum narrows with  $E$ ). As a result, i) energy scaling requires a huge negative GDD, ii) the soliton obtained has a large width, and iii) it is not compressible linearly.

In contrast to the soliton regime, the pulse is stretched in the PDR [19] and its peak power is reduced due to chirp  $\psi$  [20, 21]. The chirp compensates the narrowing of the spectrum with energy [20]:

$$2\Delta \approx 8\pi\psi/\gamma E, \quad (3)$$

where  $\Delta$  is the spectrum half-width. The advantage is that such a pulse (chirped solitary pulse, CSP) is compressible linearly down to  $T \approx 2/\Delta$  (the compression factor is  $\approx \psi$ ).

As was found, the CSP can be described as a solitary pulse solution of the cubic nonlinear complex Ginzburg-Landau equation (CGLE) [21] or, more generally, the cubic-quintic nonlinear CGLE [20, 26, 27, 28]. This equation is the generalized form of the master mode-locking equation [17, 21, 22, 23], which provides an adequate description of mode-locked oscillators (both fiber and solid-state). Besides, the nonlinear CGLE is used in quantum optics, modeling of Bose-Einstein condensation, condensate-matter physics, study of non-equilibrium phenomena, and nonlinear dynamics, quantum mechanics of self-organizing dissipative systems, and quantum field theory [24]. Therefore, analysis of the CSP solutions of nonlinear CGLE is of interest not only from the practical but also from the theoretical point of view.

Since the underlying problem is multiparameter and not integrable in the general form, there is no a uniform standpoint on CSPs developing in, for example, the ANDi fiber oscillator [29] and the chirped-pulse oscillator (CPO) [12]. In particular, the physical parameters of oscillators vary greatly and it is not clear a priori whether the mechanisms governing the PDR are unified.

In this work, we propose an approximate method of integrating the generalized nonlinear

CGLE and show that the CSP is its two-parametrical solitary pulse solution. As a result, the CSP characteristics are easy to trace on a two-dimensional diagram (“master diagram”). Comparison of the PDR parameters demonstrates that the CSPs formed in the ANDi fiber oscillator and in the CPO i) lie within distinct sectors of the unified master diagram, ii) belong to mainly distinct branches of solution, and iii) vary with the parameters in different ways. The variation of the main CPO characteristics (spectrum shape and width as well as pulse stability) with the PDR parameters is analyzed along with the numerical and experimental results. A comparison of the models based on the different versions of the master equation is made.

## II. CSP SOLUTION OF THE GENERALIZED NONLINEAR CGLE

The evolution of the visible, near- and mid-infrared electromagnetic fields in an oscillator can be described on the basis of the slowly-varying field approximation, when the spectral width is much smaller than the carrier frequency of the field. The field envelope  $A$  is affected mainly by i) GDD, ii) SPM (non-dissipative factors), as well as iii) saturable gain and linear loss, iv) spectral filtering, and v) self-amplitude modulation (SAM) (dissipative factors) [17, 22]. When the effects of higher-order dispersion [25] and the field variation along a single oscillator round-trip [20] are negligible, the oscillator dynamics obeys the nonlinear CGLE:

$$\frac{\partial A}{\partial z} = \sigma A + (\alpha + i\beta) \frac{\partial^2 A}{\partial t^2} + \left( \frac{\mu\varsigma}{1 + \varsigma |A|^2} - i\gamma \right) |A|^2 A, \quad (4)$$

where  $z$  is the propagation distance normalized to the oscillator length (for a ring oscillator model; or to double its length for a linear oscillator),  $t$  is the local time (the reference frame is co-moving with a solitary pulse solution of Eq. (4)),  $\sigma = g - l - \mu$  is the dimensionless saturated net gain ( $g$ ,  $l$  and  $\mu$  are the saturated gain, non-saturable and saturable loss coefficients, respectively),  $\alpha$  is the squared inverse transmission bandwidth of an oscillator,  $\beta$  is the GDD coefficient,  $\varsigma$  is the inverse saturation power of the self-amplitude modulator (SAM),  $\gamma$  is the net SPM coefficient. The normalization of the slowly varying field amplitude  $A(z, t)$  is chosen such that  $P(z, t) \equiv |A|^2$  is the instantaneous power. The SAM corresponds to a perfectly saturable absorber. For instance, it can be a semiconductor saturable mirror (SESAM) operating under the condition of a substantial pulse width (few picoseconds for

the PDR) excess over the SESAM relaxation time ( $\approx 100$  femtoseconds) [30].

Rescaling  $z' = z\mu$ ,  $t' = t\sqrt{\mu/\beta}$ , and  $P' = \zeta P$  demonstrates that Eq. (4) is in fact three-parametrical. However, as will be demonstrated below, the CSP is the two-parametrical solution of Eq. (4). In contrast to Ref. [28], we do not impose restrictions on the pulse phase  $\phi(t)$ :

$$A(z, t) = \sqrt{P(t)} \exp(i\phi(t) - iqz), \quad (5)$$

where  $q$  is the phase produced by slip of the carrier phase in relation to the slowly varying envelope  $\sqrt{P(t)}$  [17].

By analogy with Refs. [20, 27], substitution of Eq. (5) in Eq. (4) with the subsequent assumptions  $\alpha \ll \beta$  (GDD prevails over spectral dissipation), and  $d^2\sqrt{P}/dt^2 \ll 1$  (that is, the adiabatic approximation  $\beta \ll T^2$ ) results in

$$\begin{aligned} \gamma P(t) &= q - \beta \Omega(t)^2, \\ \beta \frac{d\Omega(t)}{dt} + \beta \frac{\Omega(t)}{P(t)} \frac{dP(t)}{dt} &= \sigma + \frac{\mu \zeta P(t)}{1 + \zeta P(t)} - \alpha \Omega(t)^2, \end{aligned} \quad (6)$$

where  $\Omega(t) \equiv d\phi(t)/dt$  is the instant frequency.

The regularity conditions  $P(t) > 0$  and  $d\Omega/dt < \infty$  require spectrum truncation so that  $\Omega(t)^2 < \Delta^2 \equiv q$ :

$$\begin{aligned} \zeta P(0) &= \frac{\alpha \Delta^2}{\mu b} = \frac{3}{4b} \left[ 2(1+a) - b \pm \sqrt{\Upsilon} \right], \\ \frac{d\Omega}{dt} &= \frac{\alpha}{3\beta} \frac{(\Xi^2 - \Omega^2)(\Delta^2 - \Omega^2)}{\Delta^2 - \Omega^2 + \gamma/\zeta\beta}, \\ \frac{\alpha \Xi^2}{\mu} &= \frac{2\alpha}{3\mu} \Delta^2 + 1 + a + b. \end{aligned} \quad (7)$$

Here  $a \equiv \sigma/\mu$ ,  $b \equiv \alpha\gamma/\beta\zeta\mu$ ,  $\Upsilon \equiv (b-2)^2 + 4a(2+a+b)$ . Positivity of  $\Upsilon$  requires  $b < 2 - 2a - 4\sqrt{-a}$ ;  $-1 < a < 0$ . The condition  $a < 0$  provides stability against continuum growth, and the inequality  $a > -1$  means that  $\sigma$  cannot exceed the SAM depth. The positive (“+” sign in the first Eq. (7)) and negative (“-” sign) branches of the solution (7) coincide along the curve  $P(0) = 3[2(1+a) - b]/4b\zeta = 3(\sqrt{2b} - b)/2b\zeta$ .

Integration of Eq. (7) results in the implicit expression for the CSP profile

$$t = \frac{3}{\alpha\zeta\Delta\Xi(\Xi^2 - \Delta^2)} \left\{ [(\Xi^2 - \Delta^2)\beta\zeta - \gamma] \Delta \operatorname{arctanh}\left(\frac{\Omega}{\Xi}\right) + \gamma\Xi \operatorname{arctanh}\left(\frac{\Omega}{\Delta}\right) \right\}. \quad (8)$$

where  $\Omega$  has to be interpreted in the sense of the first of Eq. (6). Equation (8) allows the spectral chirp to be expressed as

$$\Psi \equiv \frac{d^2\phi(\omega)}{d\omega^2} = \frac{3\beta}{2\alpha} \frac{\Delta^2 - \omega^2 + \gamma/\beta\varsigma}{(\Xi^2 - \omega^2)(\Delta^2 - \omega^2)}. \quad (9)$$

The frequency dependence of  $\Psi$  defines the CSP compressibility [27, 34]: parts of the spectrum where the chirp is strongly frequency-dependent, belong to the pulse satellites after pulse compression. The flatness of the chirp in the vicinity of  $\omega = 0$  enhances as the stability border  $\sigma = 0$  is approached. In contrast to the case of Ref. [20], the chirp is always minimum at the central frequency  $\omega = 0$ .

The next step is to assume that  $\phi(t)$  is a rapidly varying function for the CSP [20, 27]. The stationary-phase method of [27, 33] allows one to express the spectral power from the first of Eqs. (6):

$$p(\omega) \equiv \left| \int_{-\infty}^{\infty} dt \sqrt{P(t)} e^{i\phi(t) - i\omega t} \right|^2 \approx \frac{6\pi\beta^2}{\gamma\alpha} \frac{\Delta^2 - \omega^2 + \gamma/\varsigma\beta}{\Xi^2 - \omega^2} \Theta(\Pi^2 - \omega^2), \quad (10)$$

where  $\Theta(x)$  is the Heaviside function and  $\Pi = \min\{\Delta, \Xi\}$  is the least of  $\Delta$  and  $\Xi$ . Equation (10) demonstrates that the CSP has the spectrum truncated at  $\pm\Pi$  (i.e.  $|\omega| < \Pi$ ).

Integration of Eq. (10) allows the pulse energy to be expressed as

$$E \equiv \int_{-\infty}^{\infty} P(t) dt \approx \int_{-\Delta}^{\Delta} p(\omega) \frac{d\omega}{2\pi} = \frac{6\beta^2\Delta}{\alpha\gamma} \left[ 1 - \frac{(\Xi^2 - \Delta^2 - \gamma/\beta\varsigma) \operatorname{arctanh}\left(\frac{\Delta}{\Xi}\right)}{\Delta\Xi} \right]. \quad (11)$$

It is clear from Eq. (11) that the truncation parameter  $\Pi$  is equal to  $\Delta$ , i.e.  $\Delta < \Xi$ . In contrast to the cubic-quintic CGLE, whose solution is the truncated Lorentz function in the spectral domain [20], the spectrum in our case is parabolic-top ( $\Delta < \Xi$ ): i) convex if  $\alpha\Delta^2 < 3(\mu + \sigma)$ , ii) flat-top if  $\alpha\Delta^2 = 3(\mu + \sigma)$ , and iii) concave if  $\alpha\Delta^2 > 3(\mu + \sigma)$ .

In an oscillator, the  $\sigma$ -( $a$ -)parameter is energy-dependent owing to saturation of the gain  $g$ . The simplest law of saturation is  $g = g(0)/(1 + E/E_s)$  [23], where  $g_0$  is the gain for

TABLE I: Relations between dimensional and dimensionless quantities

$E$	$E' \beta^2 \sqrt{\mu}/\gamma\alpha\sqrt{\alpha}$
$E^*$	$E^{*'} \beta^2 \sqrt{\mu}/\gamma\alpha\sqrt{\alpha}$
$P$	$P'/\varsigma$
$p$	$p' \beta^2 / \alpha \gamma$
$\omega$	$\omega' \sqrt{\mu/\alpha}$
$\Omega$	$\Omega' \sqrt{\mu/\alpha}$
$\Delta$	$\Delta' \sqrt{\mu/\alpha}$
$\Xi$	$\Xi' \sqrt{\mu/\alpha}$
$\Psi$	$\Psi' \beta / \mu$

a small signal (unsaturated gain) and  $E_s$  is the saturation energy. This expression can be expanded in the vicinity of  $\sigma = 0$ :

$$\sigma(E) \approx \delta(E - E^*). \quad (12)$$

The  $E^*$ -parameter is the energy defined as the averaged power of a free-running oscillator multiplied by the cavity period  $T_{cav}$ .  $E^* = (g(0) - l - \mu) E_s / (l + \mu)$  for the law of gain saturation under consideration.  $\delta \equiv d\sigma/dE|_{E=E^*}$  (i.e.  $\delta = -(l + \mu)^2 / g(0) E_s$ ). For the considered law of gain saturation, one has  $\rho \equiv E^* \delta = -g(0) (\xi - 1) / \xi^2$ , and  $\xi \equiv g(0) / (l + \mu) \approx g(0) / l$  is the pump-to-threshold ratio.

The normalizations presented in Table I reduce the three-parametrical space of Eq. (4) to a two-parametrical one  $(a, b)$  for the CSP. The resulting dimensionless equations are shown in Table II. Thus, the CSP is easily traceable on a two-dimensional plane (“master diagram”) as in the case of the nonlinear cubic-quintic CGLE [20, 27].

### III. CHIRPED-PULSE OSCILLATORS: COMPARATIVE ANALYSIS

The master diagram on the plane  $(b, E^*)$  is shown in Fig. 1. The black curve is the stability threshold  $\sigma = 0$  (that is,  $E = E^*$ ). Above this curve, the CSP does not exist (hatched region). Along this curve, the dimensionless pulse parameters (see Tables I,II) are

TABLE II: Dimensionless equations for the CSP parameters ( $a \equiv \sigma/\mu$ ,  $b \equiv \alpha\gamma/\beta\zeta\mu$ )

---



---


$$P'(0) = \frac{3}{4b} \left[ 2(1+a) - b \pm \sqrt{\Upsilon} \right]$$

$$\Delta'^2 = \frac{3}{4} \left[ 2(1+a) - b \pm \sqrt{\Upsilon} \right]$$

$$\Upsilon = (b-2)^2 + 4a(2+a+b)$$

$$\Xi'^2 = \frac{2}{3}\Delta'^2 + b + a + 1$$

$$\Psi' = \frac{3}{2}(\Delta'^2 - \omega'^2 + b)/(\Xi'^2 - \omega'^2) (\Delta'^2 - \omega'^2)$$

$$p' = 6\pi(\Delta'^2 - \omega'^2 + b) \Theta(\Delta'^2 - \omega'^2)/(\Xi'^2 - \omega'^2)$$

$$E' = 6\Delta' \left[ 1 - (\Xi'^2 - \Delta'^2 - b) \operatorname{arctanh}\left(\frac{\Delta'}{\Xi'}\right) \right] / \Delta' \Xi'$$


---



---

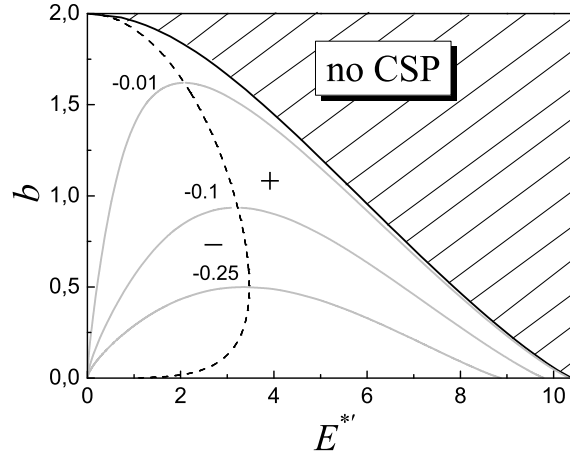


FIG. 1: The master diagram. The solid black curve is the CSP stability border. The dashed curve is the border between the “+” and “-” branches of CSP for  $\rho/\mu = 17$ . The gray curves are the isogains for  $a = -0.01$ ,  $-0.1$  and  $-0.25$  (superscribed).

$$0 < b < 2, \quad P'(0) = \Delta'^2/b = 3 \left( \frac{1}{b} - \frac{1}{2} \right), \quad \Xi'^2 = 3,$$

$$E^{*'} = 6\sqrt{3 \left( 1 - \frac{b}{2} \right)} \left[ 1 - \frac{b \operatorname{arctanh}\left(\sqrt{1 - \frac{b}{2}}\right)}{6\sqrt{1 - \frac{b}{2}}} \right]. \quad (13)$$

The dashed curve in Fig. 1 shows the border between the positive (“+”) and negative (“-”) branches of Eq. (7).

The CSPs providing a constant value of the saturated net-gain parameter  $\sigma$  correspond



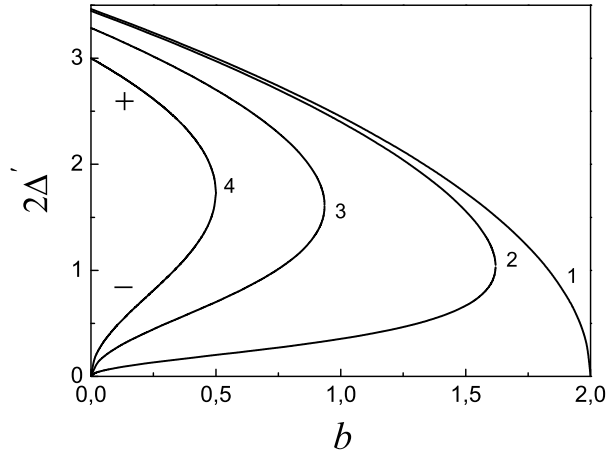


FIG. 2: The spectral widths in the isogain curves of Eq. (7) ( $a = 0$  (1),  $-0.01$  (2),  $-0.1$  (3) and  $-0.25$  (4)). The upper (lower) branches of the curves correspond to the “+”(“−”)branches of Eq. (7).

to the gray curves in Fig. 1 (so-called, “isogain” curves). The isogain  $\sigma = 0$  is the stability threshold (solid black curve), and only three non-zero isogain curves are shown (the corresponding values of  $a$  are superscribed in Fig. 1).

Since  $\sigma$  is a function of  $E/E^*$ , the isogain curves explain the meaning of the “+”- and “−” branches (see also [20]). The “+” branch corresponds to the energy-scalable CSP. This means that  $E$  grows  $\propto E^*$  along the isogain faster than the  $b$ -parameter ( $b \propto 1/\beta$ ) decreases with the dispersion  $\beta$ . That is, keeping in such an isogain with the energy scaling (note that  $E^{*'} \propto E^*/\beta^2$ ) needs a comparatively slow GDD increase. As a result, the SPM increases faster than the spectrum degrades with the GDD. That is the spectrum broadens (see Fig. 2, where  $b$ -decrease along a “+” isogain corresponds to the  $E^{*}$ -growth in Fig. 1). The spectra are broadest on the stability border.

For the “+” branch, the spectrum narrows with  $\alpha$  (Fig. 2;  $b \propto \alpha$ ). This can be explained as a result of the  $E^*$ -decrease, which is necessary for keeping in the isogain ( $E^{*'} \propto \alpha^{3/2} E^*$ ) (Fig. 1). That is, the SPM contribution decreases and the spectrum narrows.

The “−” branch corresponds to the energy-unscalable CSP. This means that  $b$ -scaling ( $b \propto 1/\beta$ ) weakly affects  $E^*$  ( $E^{*'} \propto E^*/\beta^2$ ) (Fig. 1). Thus, the energy remains almost constant along this isogain when the GDD scales. Certainly, energy scaling is possible as well. However, that is not isogain process for this branch of the CSP. For the “−” branch the spectrum narrows with the  $b$ -decrease ( $b \propto 1/\beta$ ) due to growth of the GDD contribution,

which stretches the pulse when the energy remains almost constant (Fig. 2).

When  $E^*$  changes weakly along the isogain corresponding to the “-” branch, the spectrum broadens with  $\alpha$  ( $b \propto \alpha$ ) (Fig. 2). The explanation is that the growth of spectral filtering enhances the cutoff of red (blue)-shifted spectral components located on the pulse front (tail). The spectral shift at the pulse edges is a consequence of chirp [19, 21]. The growth of cutoff shortens the CSP and, for a fixed energy,  $P_0$  increases. Since  $P_0 \propto \Delta^2$ , the spectrum broadens.

One can additionally clarify the division into the “+”- and “-” branches by considering the nonlinear cubic limit of Eq. (4). Such a limit describes a low-energy CPO [21]. In this case, the exact CSP solution is  $\propto \text{sech}(t/T)^{1+i\psi}$ , and its spectral profile can be expressed through beta functions. By the method described in the previous section it is readily found that

$$\begin{aligned}\gamma P(t) &= \beta \Delta^2 (1 - \tanh^2 [\Delta t \xi (1 + b)/3\gamma]), \\ \alpha \Delta^2 &= \frac{3\sigma b}{b - 2}, \\ p(\omega) &= \frac{6\pi\beta}{(1 + b)\xi} \Theta(\Delta^2 - \omega^2).\end{aligned}\tag{14}$$

Here  $\xi \equiv \mu\varsigma$ . Equations (14) demonstrate that i) CSP exists only for  $\sigma < 0$ , ii) its spectral width increases with  $b$  and  $|\sigma|$ . Comparison with Fig. 2 demonstrates that such behavior corresponds to the “-” branch.

On the basis of the model developed, three types of CPOs will be considered: i) all-normal-dispersion (ANDi) fiber oscillator (like that in Ref. [29]), ii) broad- (e.g. Ti:sapphire [12] or Cr:YAG [31]) and iii) narrow-band (e.g. Yb-doped [13, 14, 32]) solid-state oscillators. Representation of these on the master diagram affords a means of better understanding and controlling of CPO.

### A. ANDi fiber oscillator

In Section II, the CSP solution of the generalized nonlinear CGLE was obtained in the limits  $\alpha \ll \beta$  and  $\beta \ll T^2$ . The master parameter  $b \equiv \alpha\gamma/\beta\varsigma\mu$  controlling the CSP is defined by the relative but not absolute contributions from the dissipative and non-dissipative factors of the CGLE. This allows a unified standpoint on CPOs with parameters which vary within

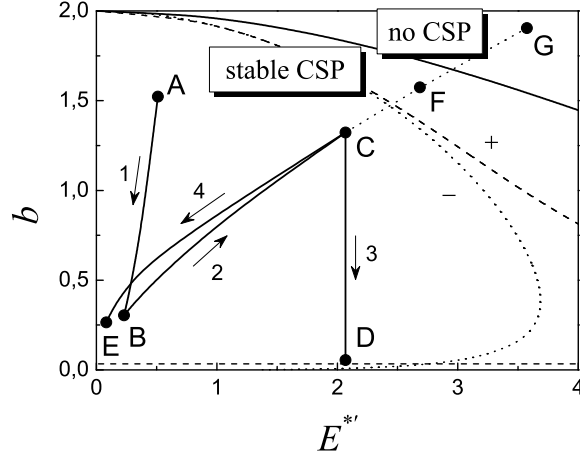


FIG. 3: Sector of master diagram (Fig. 1) representing the ANDi fiber oscillators. Parameters corresponding to the  $A$ ,  $B$ ,  $C$ ,  $D$ ,  $E$ ,  $F$ , and  $G$  points are given in Table III. The solid curve is the stability border; the dotted and dashed curves are the borders between the “+” and “-” branches of solution (7) for  $\rho/\mu = 3.8$  and  $0.76$ , respectively (i.e., respectively,  $\mu = 0.1$  and  $0.5$  for  $\rho = 0.38$ ).

a broad range.

Figure 3 shows the sector of the master diagram covering the ANDi fiber oscillator parameters (see Table III and Ref. [29]). Let us start at point  $A$  (Fig. 3 and Table III) corresponding to a typical set of ANDi-oscillator parameters but with the comparatively small SAM depth  $\mu$ . Although the GDD value is large in comparison with that in a CPO, the spectral filter bandwidth (25 nm) is small. As a result, the excess of the ratio  $\beta/\alpha$  over that for a Ti:sapphire CPO is only tenfold (see below and Ref. [20]). Simultaneously, the excess of the ratio  $\gamma/\mu\varsigma$  over that for a Ti:sapphire CPO is tenfold as well. As a result, the  $b$ -parameter is  $\sim 1$  and, dynamically, there is no substantial distinction in kind between the ANDi fiber and the solid-state CPOs. One difference is that a large GDD and a comparatively small  $E^*$  shift the operational point into the “-” branch region (Fig. 3).

Figure 4,  $A$  shows the spectrum of the numerical solution of Eq. (4) (gray circles) and the analytical profile (10) (solid curve) corresponding to point  $A$  in Fig. 3. The analytical profile reproduces the averaged numerical one. As can be seen, the numerical solution is strongly perturbed. This effect was first reported in Ref. [35] and attributed to excitation of the solitonic internal modes. Such modes grow with the GDD and are excited when the

TABLE III: Parameters of ANDi oscillator corresponding to Fig. 3.  $E^* = 12$  nJ,  $\gamma = 0.014$  W $^{-1}$ . The spectrum is centered at  $\approx 1$   $\mu$ m.

	<i>A</i>	<i>B</i>	<i>C</i>	<i>D</i>	<i>E</i>	<i>F</i>	<i>G</i>
$\alpha$ (fs $^2$ )	450	450	2000	2000	2000	2330	2820
$\beta$ (ps $^2$ )	0.1	0.1	0.1	0.1	0.5	0.1	0.1
$\mu$	0.1	0.5	0.5	0.5	0.5	0.5	0.5
$\zeta$ (kW $^{-1}$ )	0.42	0.42	0.42	10	0.42	0.42	0.42

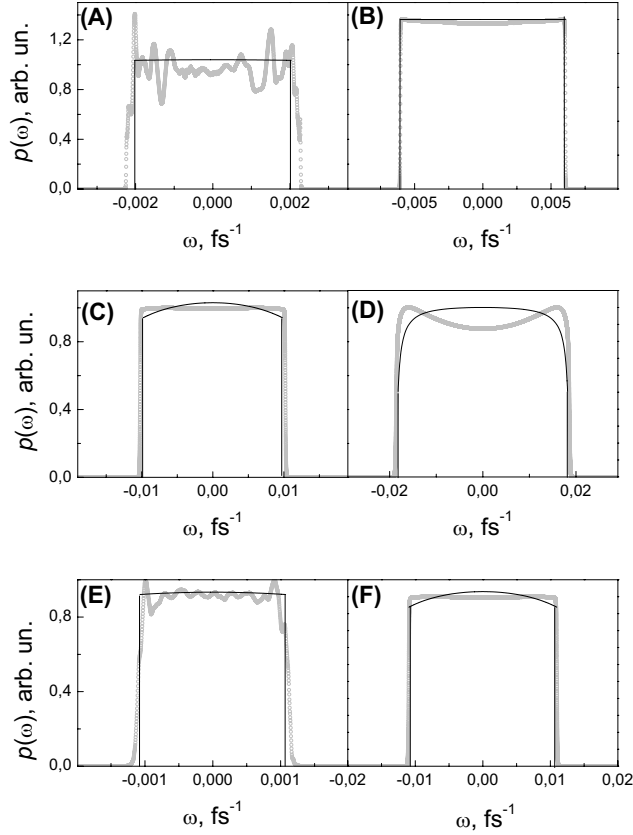


FIG. 4: Numerical (gray circles) and analytical (solid black curves) spectra of ANDi fiber oscillators with the parameters defined in Table III.  $\rho = 0.38$ .

value  $\beta/\alpha$  is large.

A way of suppressing such a perturbation is to increase the SAM depth  $\mu$  (transition 1 from *A* to *B* in Fig. 3). The  $\mu$ -growth is not the isogain process, as the  $|a|$ -parameter increases. As a result, the spectrum broadens (Fig. 4, *B*) according to the analytical model

(transition from the lower branch of curve 2 to that of 4 in Fig. 2).

An important factor governing the CPO is spectral filtering, since the pulse lengthening due to GDD has to be compensated by its shortening owing to frequency filtering of the chirped pulse [21]. In the framework of the model under consideration, the filter band narrowing can be illustrated by transition 2 to point  $C$  in Fig. 3. Such a transition results in almost isogain growth of the  $b$ -parameter. Hence, for the “-” branch of the CSP (Fig. 2) the spectrum broadens (Fig. 4,  $C$ ) [29]. The further filter band narrowing transforms the pulse into the “+” branch of the CSP (Fig. 4,  $F$ ). Further growth of  $b \propto \alpha$  due to filter band narrowing destabilizes the pulse ( $\sigma > 0$  at point  $G$ ).

The next important factor is the inverse power of the loss saturation (the SAM parameter  $\varsigma$ ). Its growth (transition 3 from  $C$  to  $D$  in Fig. 3) corresponds to the  $b$ -decrease. First, this is not an isogain process, i.e. the  $|a|$ -parameter increases, which broadens the spectrum (Fig. 2). Second, the spectrum narrows with the  $b$ -decrease for the “-” branch of the CSP (Fig. 2). In our example, point  $D$  is located in the vicinity of the border between the “-” and “+” branches of the CSP. In accordance with Figure 2, this means that the spectrum broadens owing to the  $|a|$ -parameter growth (Fig. 4,  $D$ ). Figure 4,  $D$  demonstrates that, unlike the analytical profile, the numerical one is distinctly concave. This issue will be discussed in the next section.

The characteristic of the ANDi fiber oscillator is that it is possible to vary the positive GDD within a wide range [29]. The GDD growth decreases the  $b$ -parameter and, as a result, narrows the spectrum of the CSP relating to the “-” branch (Figs. 2 and 4,  $E$ ) [29]. Such a conclusion is valid for both isogain and non-isogain variation. In the latter case, the  $|a|$ -parameter decreases with the GDD growth for a fixed  $E^*$ , which enhances the narrowing of the spectrum for the “-” branch (Fig. 2). Solitonic internal modes again occur [35] and the spectrum becomes perturbed (Fig. 4,  $E$ ).

## B. Broadband solid-state CPO

As was pointed out, there are two distinctive differences between the ANDi fiber oscillator and the solid-state CPO: the former has substantially larger GDD and SPM. Nevertheless, both oscillators can be described from a unified standpoint because their properties are defined by only two dimensionless parameters,  $b$  and  $E^*$ . From this point of view, the main

difference between them is that the ANDi oscillator belongs mainly to the “−” branch of the CSP, whereas the CPO belongs to the “+” branch. It should be noted that this statement need not be considered categorically, because the growth of SAM and spectral filtering shifts the operational point of an ANDi oscillator into the “+” branch region (see points *D* and *F* in Fig. 3).

Let us consider a broadband (Ti:sapphire) CPO with the parameters presented in Table IV. The mode-locking is provided by SESAM with the inverse saturation power  $\varsigma$ , which corresponds to a saturation energy fluence of  $100 \mu\text{J}/\text{cm}^2$ , a relaxation time of 0.5 ps and a mode radius of  $100 \mu\text{m}$ .

TABLE IV: Parameters of a Ti:sapphire CPO corresponding to Fig. 5.  $\alpha = 2.5 \text{ fs}^2$ ,  $\gamma = 4.55 \text{ MW}^{-1}$ ,  $\varsigma = 16 \text{ MW}^{-1}$ . The spectrum is centered at  $\approx 0.8 \mu\text{m}$ .

	<i>A</i>	<i>B</i>	<i>C</i>	<i>D</i>
$\beta$ (fs <sup>2</sup> )	160	160	160	180
$\mu$	0.01	0.02	0.02	0.02
$E^*$ (nJ)	1120	1120	2240	2240

The operational point *A* on the stability border (Fig. 5) corresponds to the minimum GDD and the broadest (for a given set of parameters) spectrum ( $\approx 70 \text{ nm}$ , see Fig. 6 *A*).

An attempt to increase the energy would destabilize the CSP. Therefore, at first it is useful to increase the modulation depth (transition 1 to from *A* to *B* in Fig. 5). This is not an isogain process, and therefore the spectrum (Fig. 6, *B*) does not change substantially in spite of the *b*-decrease (the *b*-decrease broadens the “+” branch spectrum, but the  $|a|$ -growth narrows it, see Fig. 2).

The increase of the inverse saturation power  $\varsigma$  (e.g. by means of mode reduction) would be useful for subsequent energy growth. However, as a rule, the SESAM operates in the vicinity of the damage threshold, and so the  $\varsigma$ -growth can be problematic.

The stability reserve obtained (point *B* in Fig. 5) allows energy scaling (transition 2 from *B* to *C* in Fig. 5). Nevertheless, the twofold energy growth destabilizes the CSP in our case, and multipulsing occurs.

The way out is to increase the GDD (transition 3 from *C* to *D* in Fig. 5), which shifts the operational point inside the stability range. Since the  $A \rightarrow D$  transition is a isogain

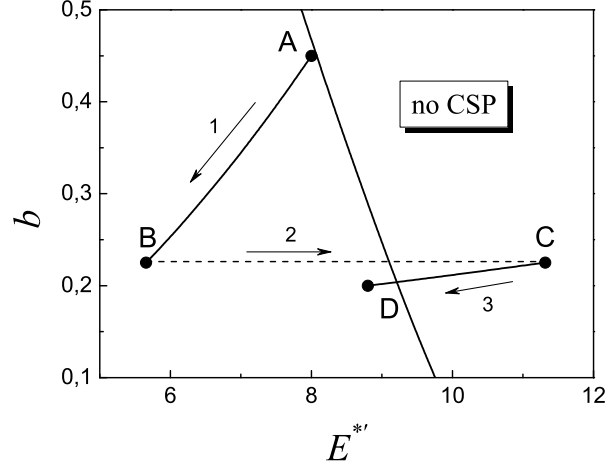


FIG. 5: Sector of master diagram (Fig. 1) representing the broadband solid-state CPOs. Parameters corresponding to points  $A$ ,  $B$ ,  $C$ , and  $D$  are given in Table IV. The solid curve is the stability border.

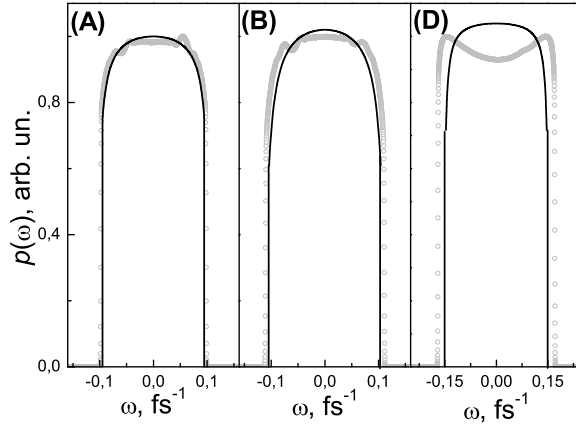


FIG. 6: Numerical (gray circles) and analytical (solid black curves) spectra of CPO oscillators with the parameters defined in Table IV.  $\rho = 0.17$ .

process following the  $b$ -decrease (curve with  $a = 0$  in Fig. 2), the spectrum broadens (Fig. 6,  $D$ ). Again, the spectrum becomes concave.

It should be noted that, in an experiment, the main control parameter used for oscillator stabilization at some fixed  $E^*$ -level is the GDD value. The GDD growth (corresponding to the  $b$ -decrease) is not an isogain process for the “+” branch of the CSP and is almost an isogain one for the “-” branch. Figure 2 shows that the spectrum narrows in the latter

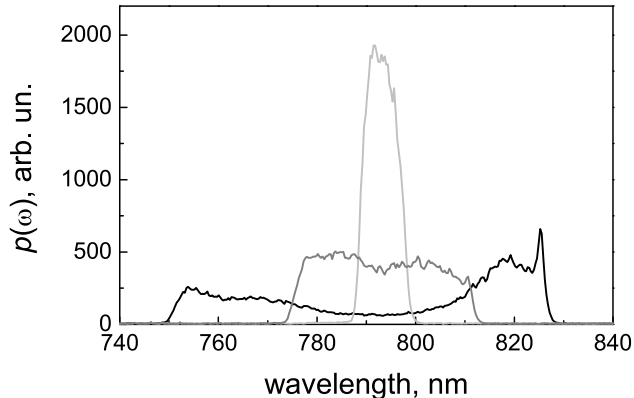


FIG. 7: Experimental spectra from the Ti:sapphire CPO corresponding to the growing positive net GDD (from the black via gray to the light gray curves). Pump power 5.5 W; 1.25 W in the mode-locked regime.

case. For the “+” branch, the  $|a|$ -parameter increases with GDD, which enhances the CSP stability against the continuum growth. From Eq. (7) it is seen that the  $|a|$ -parameter growth narrows the spectrum. Numerical simulations demonstrate that the total effect of the GDD growth in the case under consideration is narrowing of the spectrum and stretching of the CSP. Such a conclusion agrees with the experiment [12]. Figure 7 shows the spectra from the Ti:sapphire CPO corresponding to the positive net GDD growing step by step. The spectra narrow with the GDD growth and reshape from concave via flat-top to parabolic. Equation (10) reproduces the growth of convexity with narrowing of the spectrum. The concave spectra appear in the numerical simulations, when the spectrum becomes sufficiently broad (Figs. 4, *D* and 6, *D*). The analytical theory fails to reproduce this phenomenon (see Section IV).

### C. Narrowband solid-state CPO

As was found in Ref. [20], there is a limit to CPO energy growth with resonator lengthening, because the modulation depth  $\mu$  has to increase  $\propto T_{cav}/T_r$  (here  $T_r$  is the gain relaxation time). Since broadband solid-state active media such as Ti:sapphire, Cr-doped zinc-chalcogenides, and Cr:YAG have comparatively short gain relaxation times (a few mi-



croseconds), it is preferable to use media with a long relaxation time, such as Yb-doped crystals. Moreover, the cavity length realized so far is already in the MHz-range in terms of repetition rate, meaning that the only scaleable parameter remains the power. Power scaling is realizable in a Yb-doped thin-disk oscillators. For example, the Yb:YAG oscillator operating in the NDR has exceeded the 13- $\mu\text{J}$  energy frontier [8]. Such a regime requires a fair amount of negative GDD ( $\approx -0.2 \text{ ps}^2$  in the case of Ref. [8]) and the pulse obtained is linearly incompressible.

It is interesting to consider the prospects of such a regime within the PDR. The issue is that a Yb-doped medium has a comparatively narrow gainband ( $\alpha \approx 1000 \text{ fs}^2$ ) and it is not clear a priori that the CPO can operate at GDD levels close to  $\alpha$ . Nevertheless, Yb-doped CPOs have been demonstrated experimentally [13, 14]. The CSPs obtained were compressible down to  $\approx 450 \text{ fs}^2$  and the positive net GDD varied within the range  $\approx 250 - 2250 \text{ fs}^2$ .

Let us consider a Yb:YAG thin-disk CPO mode-locked by SESAM and aiming at an intracavity pulse energy level  $\approx 80 \mu\text{J}$ . At such an energy level, an important factor is the SPM due to air filling the resonator [7]. Such a factor has to be taken into account. Let the cavity length be 15 m, and the averaged mode diameter be equal to 2.4 mm. The Yb:YAG-disk thickness is 0.4 mm. The SESAM saturation energy fluence is  $100 \mu\text{J}/\text{cm}^2$ , its relaxation time is 0.6 ps, and the mode diameter on SESAM is 1.2 mm. Other parameters are presented in Table V.

TABLE V: Parameters of a Yb:YAG CPO:  $\alpha = 900 \text{ fs}^2$ ,  $\varsigma = 0.53 \text{ MW}^{-1}$ ,  $\mu = 0.005$ ,  $E^* = 80 \mu\text{J}$ . The spectrum is centered at  $\approx 1 \mu\text{m}$ .

	$A$	$B$	$C$
$\beta \text{ (fs}^2\text{)}$	2550	700	2900
$\gamma \text{ (GW}^{-1}\text{)}$	1.9	0.15	2.4

Point  $A$  in Fig. 8 corresponds to the narrowband CPO operating in the vicinity of the stability border. The CPO resonator is filled with air. The CSP belongs to the “+” branch; the corresponding spectrum is shown in Fig. 9,  $A$ . Its width is  $\approx 3.5 \text{ nm}$ , which allows compressing linearly down to  $\approx 300 \text{ fs}$ . Although the ratio  $\beta/\alpha$  is only 2.8, the analytical profile provides quite precise fitting of the numerical spectrum.

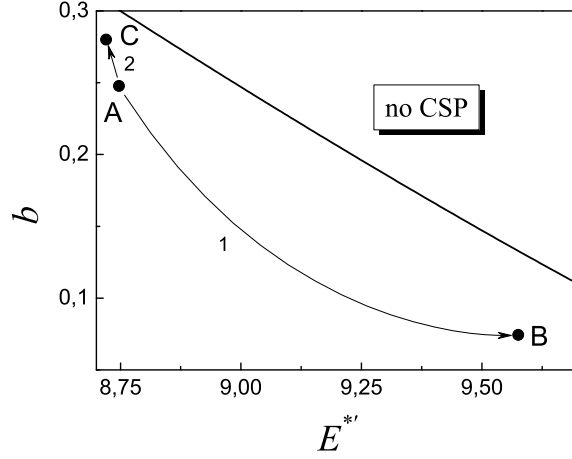


FIG. 8: Sector of master diagram (Fig. 1) representing the narrowband solid-state CPOs. Parameters corresponding to points  $A$ ,  $B$ , and  $C$  are given in Table V. The solid curve is the stability border.

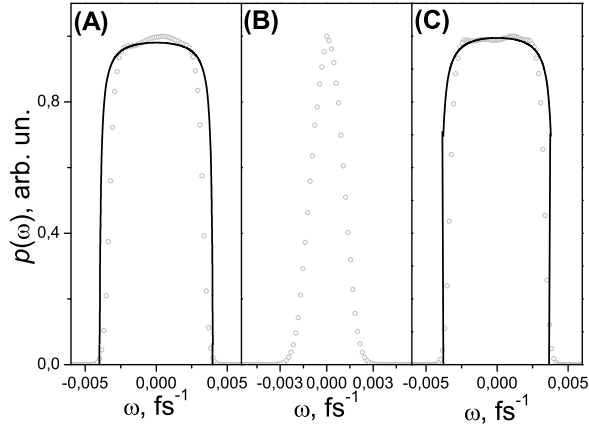


FIG. 9: Numerical (gray circles) and analytical (solid black curves) spectra of CPO oscillators with the parameters defined in Table V.  $\rho = 0.05$ .

Violation of the assumption of  $\beta \gg \alpha$  underlying the analytical model results in smoothed spectrum edges. Such smoothing increases (Fig. 9,  $B$ ) when the resonator becomes airless and only the active medium nonlinearity contributes to the oscillator dynamics. Point  $B$  in Fig. 8 corresponds to the neighborhood of the analytical stability border, i.e. the almost

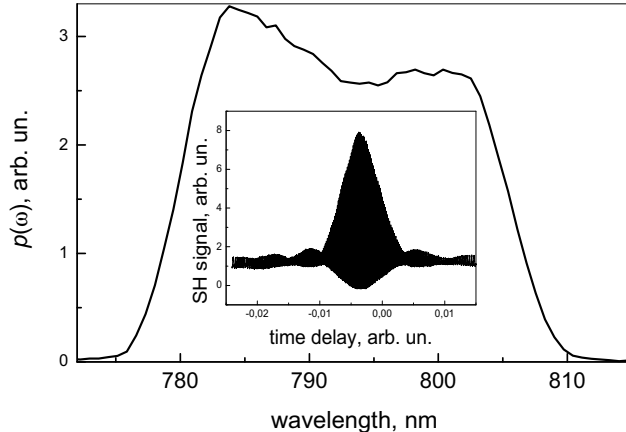


FIG. 10: Experimental spectrum and autocorrelation function (inset) from the Ti:sapphire CPO mode-locked by SESAM. Repetition rate 60 MHz, intracavity energy 200 nJ.

minimum possible GDD value providing the broadest spectrum. Since  $\beta < \alpha$ , the analytical model is not valid, although the pulse is chirped and remains almost fourfold compressible (down to  $\approx 800$  fs).

The net-gainband narrowing (growth of  $\alpha$  in comparison with  $\beta$ ) can also result from spectral filtering produced by comparatively narrowband SESAM. In this case, the  $\alpha$ -parameter is defined by the SESAM bandwidth, and the approach of the  $\alpha$ -parameter to the  $\beta$ -parameter results in smoothing of the spectrum edges in a Ti:sapphire oscillator as well (Fig. 10).

Spectrum control of the narrowband CPO operating in the vicinity of the stability border can be provided by inserting a plate (e.g., a sapphire plate) introducing additional SPM (point  $C$  in Fig. 8; 0.1-cm sapphire plate). Figure 9,  $C$  demonstrates that the  $b$ -growth ( $b \propto \gamma$ ) provides excellent agreement between the numerical and analytical solutions.

It can be concluded that the absolute value of GDD required for high-energy pulse stabilization is substantially lower in the PDR than that in the NDR, so that one can avoid the resonator helium filling or vacuumization of the resonator. Nevertheless, vacuumization of the oscillator can provide the most direct way to substantial energy growth. Let us consider an example with an intracavity energy of  $\approx 0.8$  mJ for a configuration corresponding to point  $C$  in Fig. 8. The scaling rules  $E^* = E^* \gamma \alpha^{3/2} / \sqrt{\mu} \beta^2$ ,  $b = \alpha \gamma / \beta \zeta \mu$  (Table I) demonstrate that tenfold reduction of SPM (as a result of resonator vacuumization) and SAM (as a result of for instance, mode growth and/or reduction of the saturation energy fluence) allow the

system to be kept at point  $C$ . This guarantees that the dynamics is preserved. However, the direct way can be unusable due to  $P_0$ -growth. One can then increase  $\beta$  and, simultaneously, decrease the modulation depth  $\mu$  as well as  $\zeta, \gamma$  (e.g. by means of mode growth in a gas-filled resonator) in accordance with the scaling rules but keeping  $P_0$  below  $P_{th}$ .

#### IV. BRIEF COMPARISON OF THE MODELS

Section II reports the development of a model of a CPO mode-locked by an ideally saturable absorber. Such a model is applicable to both the ANDi fiber oscillator [29] and solid-state CPO mode-locked by SESAM. Simultaneously, there are models of a CPO based on the nonlinear cubic-quintic CGLE [20, 28, 34, 36]. Such models take into account the SAM saturation (i.e. the decrease of SAM with power overgrowth), which is important in high-power Kerr-lens mode-locked oscillators as well as fiber oscillators mode-locked by a polarization modulator. Finally, the low-energy sector (as well as the large positive GDD sector) of CPO can be described by the nonlinear cubic CGLE (i.e. by dissipative generalization of the nonlinear Schrödinger equation).

Here, we consider in brief the influence of the power dependence of SAM on the CSP spectrum. It should be noted that the SAM saturation parameter is not truly a free parameter in a real-world oscillator. It is closely related to the inverse saturation power  $\varsigma$  (see [20]). Underestimation of this parameter can lead to a huge CSP spectral width and peak power (e.g. see [36]). Constraint on such a power growth can be provided by the gain saturation and, as a result of  $|a|$ -growth, the CPO operates in the “−” branch of CPO (in terms of this article, see above). To stabilize the CPO against the internal perturbations [35], the SAM parameter has to be increased. Switching to the “+” branch of the CPO can be provided by i) GDD decrease, ii) energy growth, or iii) spectral filter band narrowing. This can result in collapse-like instability of the CSP if there is no SAM saturation, or in the continuum growth for  $\sigma > 0$  (see Fig. 1).

An important issue is the appearance of concave spectra like those in Figs. 4,  $D$  and 6,  $D$ . It is known that, for the SAM described by the nonlinear cubic-quintic CGLE, the CSP has either parabolic- or finger-top spectra [20]. The analytical concave spectrum appears only for SAM, which enhances the collapse-like instability (i.e. there is no SAM saturation) [28]. However, such spectra are observable both numerically [28, 36] and experimentally [28, 29].

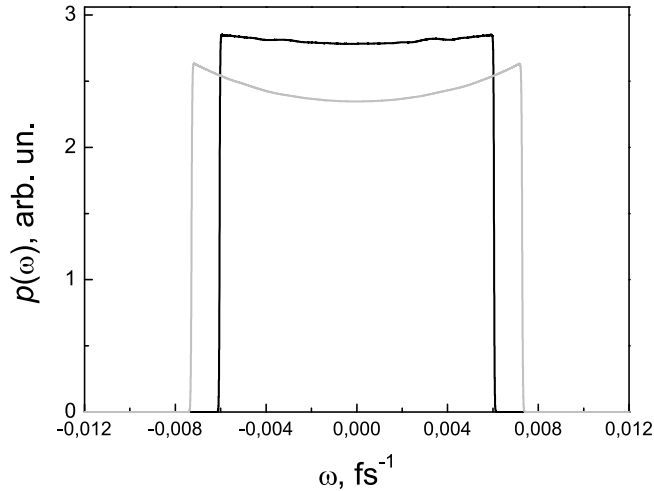


FIG. 11: Numerical spectral profiles corresponding to the model (4) (black curve) and its nonlinear cubic limit (gray curve). Parameters correspond to the point *B* in Fig. 3.

For the SAM type considered in the present work, there exist analytical concave spectral profiles (see Eq. (10)). However, it can be concluded from Eq. (7) that such solutions are nonphysical.

Figures 4, 6 show that the concavity grows with spectrum broadening when  $1/(2\Delta)^2$  tends to  $\alpha$ . Simultaneously, there is no concave spectrum, when SPM is suppressed (Fig. 9, where  $\gamma < \mu\varsigma$ ).

Numerical analysis demonstrates that the appearance of a concave spectrum is not rooted in the character of SAM. Surprisingly, however, the concave spectrum profile exists even in the case of the nonlinear cubic CGLE and develops with the spectrum broadening. Figure 11 shows the spectra corresponding to point *B* in Fig. 3, but for the different SAM types:  $\mu\varsigma |A|^2 / (1 + \varsigma |A|^2)$  (black curve, see Eq. (4)) and  $\mu\varsigma |A|^2$  (nonlinear cubic model, gray curve). It can be seen that the absence of SAM saturation in the second case leads to spectrum broadening due to power growth ( $\Delta^2 \propto P(0)$ , see Eqs. (7,14)). Analytical estimation for  $\Delta$  from Eq. (14) gives  $0.0076 \text{ fs}^{-1}$  vs. numerical value  $0.0074 \text{ fs}^{-1}$ . As a result of the spectrum broadening, the concavity increases. The  $P(t)$ -profile does not have any anomalies. Thus, growth of spectral components at the spectrum edges can be treated as a fundamental feature of the regime considered (see also Ref. [35]), without obligatory addressing of higher-order dispersions [25].

## V. CONCLUSIONS

Analytical theory of the CSP has been developed. The theory treats the CSP as a solitary pulse solution of the generalized nonlinear CGLE. The main advantage of the theory developed is the possibility of representing the CPO parametrical space in the form of a two-dimensional master diagram. As a result, the CSP characteristics become easily traceable. It has been demonstrated that both ANDi fiber and chirped-pulse solid-state oscillators can be described from a uniform standpoint and represented on a unified master diagram. The main difference between them is that they realize mainly two different branches of the CSP solution. Such branches differ in the energy and dispersion scaling rules as well as in the behavior of the CSP parameters.

Comparison with the results of numerical simulations has shown that the analytical solution provides a good approximation of the spectrum shape, which is truncated and has a flat or parabolic top. The approximation is quite precise even in the case where the net-gainband is so narrow that the squared inverse bandwidth verges towards the GDD. This provides an adequate description of both ANDi fiber and thin-disk narrowband solid-state chirped-pulse oscillators. Thus, the theory allows the CPO characteristics to be optimized and demonstrates the feasibility of at least, sub-mJ energy scaling in a thin-disk CPO.

### Acknowledgments

This work was supported in part by Deutsche Forschungsgemeinschaft through the DFG cluster of excellence Munich Centre for Advanced Photonics ([www.munich-photonics.de](http://www.munich-photonics.de)). Author V.L.K. acknowledges support from the Max Planck Society (Germany) and Austrian Fonds zur Förderung der wissenschaftlichen Forschung (projects P17973 and P20293).

- 
- [1] Y.Lin, S.Tschuch, A.Rudenko, M.Dürr, M.Siegel, U.Morgner, R.Moshhammer, J.Ullrich, *Phys. Rev. Lett.* **101**, 053001 (2008).
  - [2] T.Südmeyer, S.V.Marchese, S.Hashimoto, C.R.E.Baer, G.Gingras, B.Witzel, U.Keller, *Nature Photonics* **2**, 599 (2008).
  - [3] S.H.Cho, B.E.Bouma, E.P.Ippen, J.G.Fujimoto, *Opt. Lett.* **24**, 417 (1999).

- [4] A.Apolonski, A.Poppe, G.Tempea, C.Spielmann, T.Udem, R.Holzwarth, T.Hänsch, F.Krausz, *Phys. Rev. Lett.* **85**, 740 (2000).
- [5] J. Aus der Au, G. J. Spühler, T. Südmeyer, R. Paschotta, R. Hövel, M. Moser, S Erhard, M. Karzewski, A. Gissen, U. Keller, *Opt. Lett.* **25**, 859 (2000).
- [6] A.Fernández, A.Verhoef, V.Pervak, G.Lermann, F.Krausz, A.Apolonski, *Appl. Phys. B: Lasers Opt.* **87**, 395 (2007).
- [7] S.V.Marchese, T.Südmeyer, M.Golling, R.Gränge, U.Keller, *Opt. Lett.* **31**, 2728 (2006).
- [8] J.Neuhaus, J.Kleinbauer, A.Killi, S.Weiler, D.Sutter, T.Dekorsky, *Opt. Lett.* **33**, 726 (2008).
- [9] S.H.Cho, F.X.Kärtner, U.Morgner, E.P.Ippen, J.G.Fujimoto, J.E.Cunnigham, W.H.Knox, *Opt. Lett.* **26**, 560 (2001).
- [10] A.M.Kowalevicz, A.Tucay Zare, F.X.Kärtner, J.G.Fujimoto, S.Dewald, U.Morgner, V.Scheuer, G.Angelow, *Opt. Lett.* **28**, 1597 (2003).
- [11] A.Fernandez, T.Fuji, A.Poppe, A.Fürbach, F.Krausz, A.Apolonski, *Opt. Lett.* **29**, 1366 (2004).
- [12] S.Naumov, A.Fernandez, R.Graf, P.Dombi, F.Krausz, A.Apolonski, *New J. Phys.* **7**, 216 (2005).
- [13] G.Palmer, M.Schultze, M.Siegel, M.Emons, U.Bünting, U.Morgner, *Opt. Lett.* **33**, 1608 (2008).
- [14] G.Palmer, M.Emons, M.Siegel, A.Steinmann, M.Schultze, M.Lederer, U.Morgner, *Optics Express* **15**, 16017 (2008).
- [15] A.Chong, J.Buckley, W.Renninger, F.Wise, *Optics Express* **14**, 10095 (2006).
- [16] B.Ortaç, O.Schmidt, T.Schreiber, J.Limpert, A.Hideur, A.Tünnermann, In: *Advanced Solid-State Photonics on CD-ROM* (The Optical Society of America, Washington, DC) ME2 (2008).
- [17] F.X.Kärtner (Ed.), *Few-cycle Laser Pulse Generation and its Applications* (Springer, Berlin, 2004).
- [18] G.Agrawal, *Nonlinear Fiber Optics* (Academic Press, San Diego, 2006).
- [19] B.Proctor, E.Westwig, F.Wise, *Optics Lett.* **18**, 1654 (1993).
- [20] V.L.Kalashnikov, E.Podivilov, A.Chernykh, A.Apolonski, *Appl. Phys. B: Lasers Opt.* **83**, 503 (2006).
- [21] H.A.Haus, J.G.Fujimoto, E.P.Ippen, *J. Opt. Soc. Am. B* **8**, 2068 (1991).
- [22] N.N.Akhmediev, A.Ankiewicz, *Solitons: Nonlinear Pulses and Beams* (London: Chapman

- and Hall, 1997).
- [23] H.A.Haus, J.G.Fujimoto, E.P.Ippen, IEEE J. Quantum Electron. **28**, 2086 (1992).
  - [24] I.S.Aranson, L.Kramer, Rev. Mod. Phys. **74**, 99 (2002).
  - [25] V.L.Kalashnikov, A.Fernández, A.Apolonski, Optics Express **16**, 4206 (2008).
  - [26] J.M.Soto-Crespo, N.N.Akhmediev, V.V.Afanasjev, S.Wabnitz, Phys. Rev. E **55**, 4783 (1997).
  - [27] E.Podivilov, V.L.Kalashnikov, JETP Lett. **82**, 524 (2005).
  - [28] W.H.Ronninger, A.Chong, F.W.Wise, Phys. Rev. A **77**, 023814 (2008).
  - [29] A.Chong, W.H.Ronninger, F.W.Wise, J. Opt. Soc. Am. B **25**, 140 (2008).
  - [30] H.A.Haus, Y.Silberberg, J. Opt. Soc. Am. B **2**, 1237 (1985).
  - [31] E.Sorokin, V.L.Kalashnikov, J.Mandom, G.Guelachvili, N.Picqué, I.T.Sorokina, New J. Physics **10**, 083022 (2008).
  - [32] M.Siegel, G.Palmer, M.Emons, M.Schultze, A.Ruehl, U.Morgner, Optics Express **16**, 14314 (2008).
  - [33] F.W.J.Olver, *Asymptotics and Special Functions* (Academic Press, New York, 1974).
  - [34] V.L.Kalashnikov, E.Podivilov, A.Chernykh, S.Naumov, A.Fernandez, R.Graf, Apolonski, New Journal of Physics **7**, 217 (2005).
  - [35] V.L.Kalashnikov, A.Chernykh, Phys. Rev. A **75**, 033820 (2007).
  - [36] N.Akhmediev, J.M.Soto-Crespo, Ph.Grelu, Physics Letters A **372**, 3124 (2008).